Natural Resources Canada | Ressources naturelles Canada

GEOLOGICAL SURVEY OF CANADA
OPEN FILE 9229

Thermochemical structure of Canada using multi-observable probabilistic inversion

R. Dave and A.J. Schaeffer

2025

Canada

GEOLOGICAL SURVEY OF CANADA
OPEN FILE 9229

Thermochemical structure of Canada using multi-observable probabilistic inversion

R. Dave and A.J. Schaeffer

2025

Recommended citation
Dave, R. and Schaeffer, A.J., 2025. Thermochemical structure of Canada using multi-observable probabilistic inversion; Geological Survey of Canada, Open File 9229, 15 p. https://doi.org/10.4095/px8zvhra09

Publications in this series have not been edited; they are released as submitted by the author.

ISSN 2816-7155
ISBN 978-0-660-74987-7
Catalogue No. M183-2/9229E-PDF
https://doi.org/10.4095/px8zvhra09

Thermochemical Structure of Canada using Multi-Observable Probabilistic Inversion

Riddhi Dave[1,*] **and Andrew Schaeffer**[2]

[1]Geological Survey of Canada, Vancouver
[2]Geological Survey of Canada, Sidney
[*]riddhi.dave@nrcan-rncan.gc.ca

ABSTRACT

The continental lithosphere of Canada, spanning over 3000 kilometres between the Atlantic, Pacific, and Arctic Oceans, exhibits a complex tectonic history characterized by Archean cratonic blocks, Proterozoic collisional orogens, and distinctive shear zones. This study focuses on constructing comprehensive thermochemical models of the Canadian lithosphere, employing a suite of modelling codes (LitMod) that integrate multiple geophysical observables, and geochemical and mineral physical data within a rigorous thermodynamic framework. The lithospheric structure and processes are examined through a two-part inversion approach, with the first part utilizing seismic datasets (Rayleigh wave dispersion and body wave data), global reference models, elevation, geoid, and surface heat flow measurements. The study aims to overcome the limitations of single-data-driven approaches, providing holistic insights into the structural changes in the crust and upper mantle. The results are expected to advance our understanding of the lithosphere's influence on surface processes, mineral prospectivity, Glacio-Isostatic Adjustment modelling, Carbon Capture, Utilization, and Storage (CCUS), and seismic hazards, among other applications. The report outlines the methodology, data inputs, and the ongoing 1-D testing phase, emphasizing the importance of validating outputs against independent studies and xenolith data to ensure robustness. The ultimate goal is to contribute to a comprehensive physical model of the Canadian lithosphere with broader implications for Earth sciences and various industries.

1 Plain Language Summary

This study explores the geological history and structure of the Canadian subsurface. Canada's ground has a complex past with ancient rocks, collisions, and unique features that shaped it over billions of years. The researchers aim to create detailed models of Canada's subsurface using advanced computer codes. They use various data, like seismic information, elevation, and heat flow, to understand how the Earth's crust and upper layer behave. The goal is to improve our knowledge of how the deeper structures and processes influence surface activities, like mining, and to contribute to environmental efforts like Carbon Capture, Storage and Utilization. Currently, the study is in the early stages, testing and refining its models to better understand Canada's underground makeup. The results will help us grasp Earth's processes better and have practical applications in several fields.

2 Introduction

The continental lithosphere of Canada holds a rich tectonic history and displays a collage of Archean cratonic blocks interconnected by Proterozoic collisional orogens and distinctive shear zones that have shaped the region over the past 4 billion years (Figure 1). It encompasses a vast area extending for > 3000 kilometres between the Atlantic, Pacific, and Arctic Oceans, with significant variations in lithospheric structure from west to east to north.

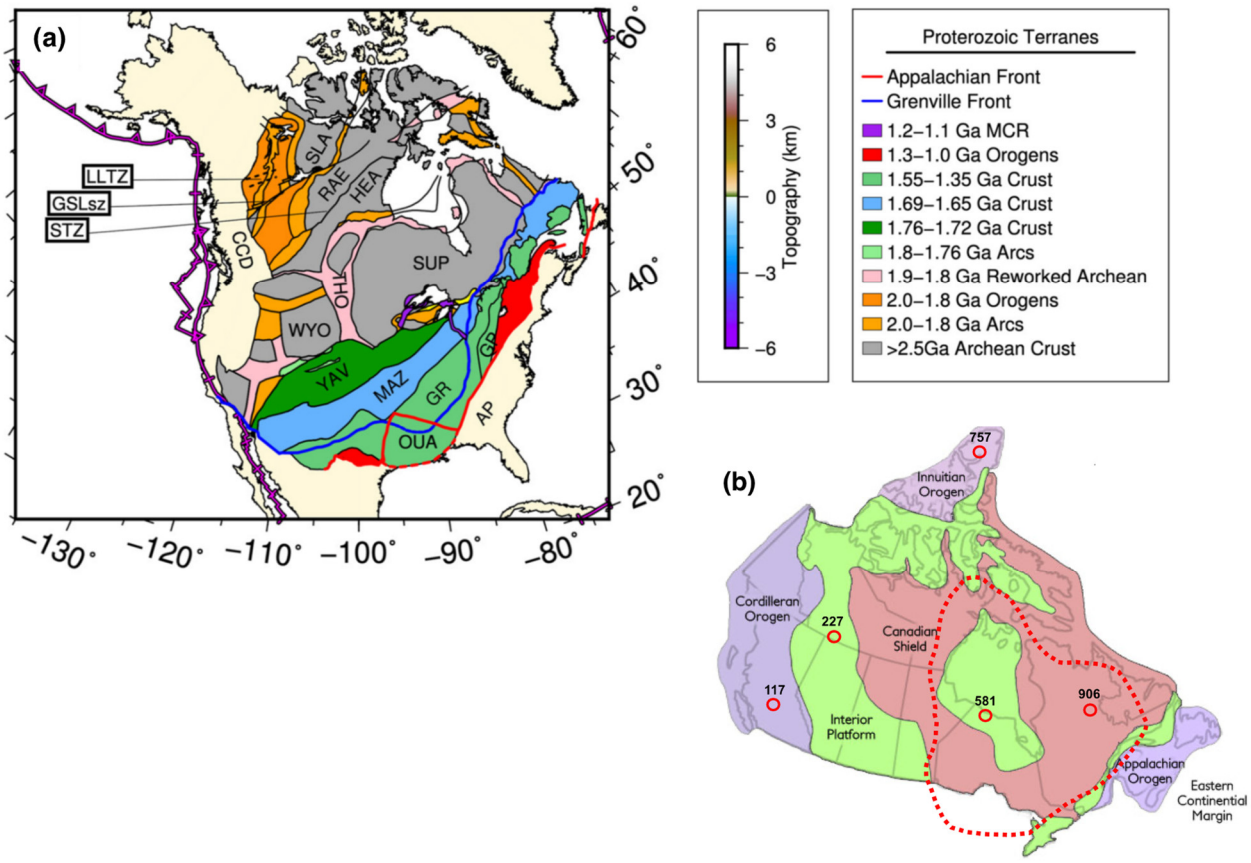

Figure 1. (a) Simplified basement geology (adapted after Whitmeyer and Karlstrom, 2007 [1]). AP: Appalachian Province, CCD: Canadian Cordillera, GP: Grenville Province, GSLsz: Great Slave Lake shear zone, HEA: Hearne craton, LLTZ: Liard Line Transfer Zone, MCR: Mid-Continent Rift, RAE: Rae craton, SLA: Slave craton, STZ: Snowbird tectonic zone, SUP: Superior craton, THO: Trans-Hudson Orogen. (b) Geological provinces of Canada with Superior province study region highlighted in red-dashed lines. The red circles and the numbers denote test grid nodes in the five geological regions.

This region can be divided into three major geological domains (Figure 1b): orogenic belts (such as the active Cordillera in the west and the inactive Appalachian and Innuitian belts in the east and north respectively), the central Archean shield, and the surrounding younger platforms, including sedimentary basins underlain by Archean rocks [2; 3; 4]. The northwesterly craton amalgamation consists of the Slave craton, the Rae craton, and the Hearne-Wyoming cratonic block [5].

During the Palaeoproterozoic Trans-Hudson Orogeny, the Superior craton collided with the amalgamation of Slave-Rae-Hearne, stretching > 4,600 kilometres from central North America to Greenland [5; 6]. The Grenville orogen bounds southeast of the Superior craton, the central North American Proterozoic terranes and subsequently the coastal Appalachian terranes [1; 7].

Present-day tectonic activity is primarily observed in the western Cordillera, which extends from California to the Alaskan Peninsula and whose formation processes are less well-understood. Here, the subduction of the Juan de Fuca and Explorer plates beneath the North American plate occurs in the south, and strike-slip motion between North America and the Pacific plate predominates further north.
The tectonic history of Canada thus varies dramatically from west to east, and there is an increased need to understand the structural changes in the crust and the upper mantle and the associated epeirogenesis experienced in these regions. The majority of the efforts in the past at constraining the lithospheric processes/features are single-data-driven approaches.

While such models have been instrumental in explaining many aspects of the lithosphere-mantle system, the intrinsic non-uniqueness and different sensitivities of these models and data do not help us converge on a comprehensive physical model of the Earth. There is abundant evidence from global studies correlating large compositional, structural, and seismic heterogeneities within the lithosphere (either crustal or mantle) with crustal manifestations in the form of topographic anomalies, major tectonic boundaries, foci of magma intrusion, and major ore deposits [8; 9; 10; 11; 12; 13; 14; 15].

Our end goal is to overcome the limitations of these single-data-driven approaches and construct holistic and comprehensive thermochemical models of the Canadian lithosphere which play a crucial role in influencing or regulating surface processes and which is seen corroborated in the global distribution of free air, geoid and isostatic anomalies [15; 16].
For this purpose, we utilize a suite of modelling codes (LitMod) which integrates multiple geophysical observables with complementary sensitivities along with geochemical and mineral physical data within a rigorous thermodynamic framework to directly image the complex feedback between structure and processes within the lithosphere [17; 18; 19]. The output results from previously constructed thermochemical models of the Superior Province (region outlined in red dashed lines in (Figure 1b) provided inferences for diamond exploration by DeBeers Inc., and have been published in various studies [20; 21; 22].

Figure 2 illustrates the two-part inversion approach utilized in this project in the form of a flowchart. We focus on the first part of the inversion in this report. The following sections will elaborate on the data inputs and the Monte-Carlo search in 1-D to construct posterior Probability Density Functions (PDF) of all parameters in the entire study region as the outcome of the first part. These posterior prediction outputs will be validated against independent studies and xenolith data to ensure robustness, and test mineral systems models thereby advancing the appraisal of mineral prospectivity. The outcome will also have applications in Glacio-Isostatic Adjustment (GIA) modelling, Carbon Capture, Utilization and Storage (CCUS), etc

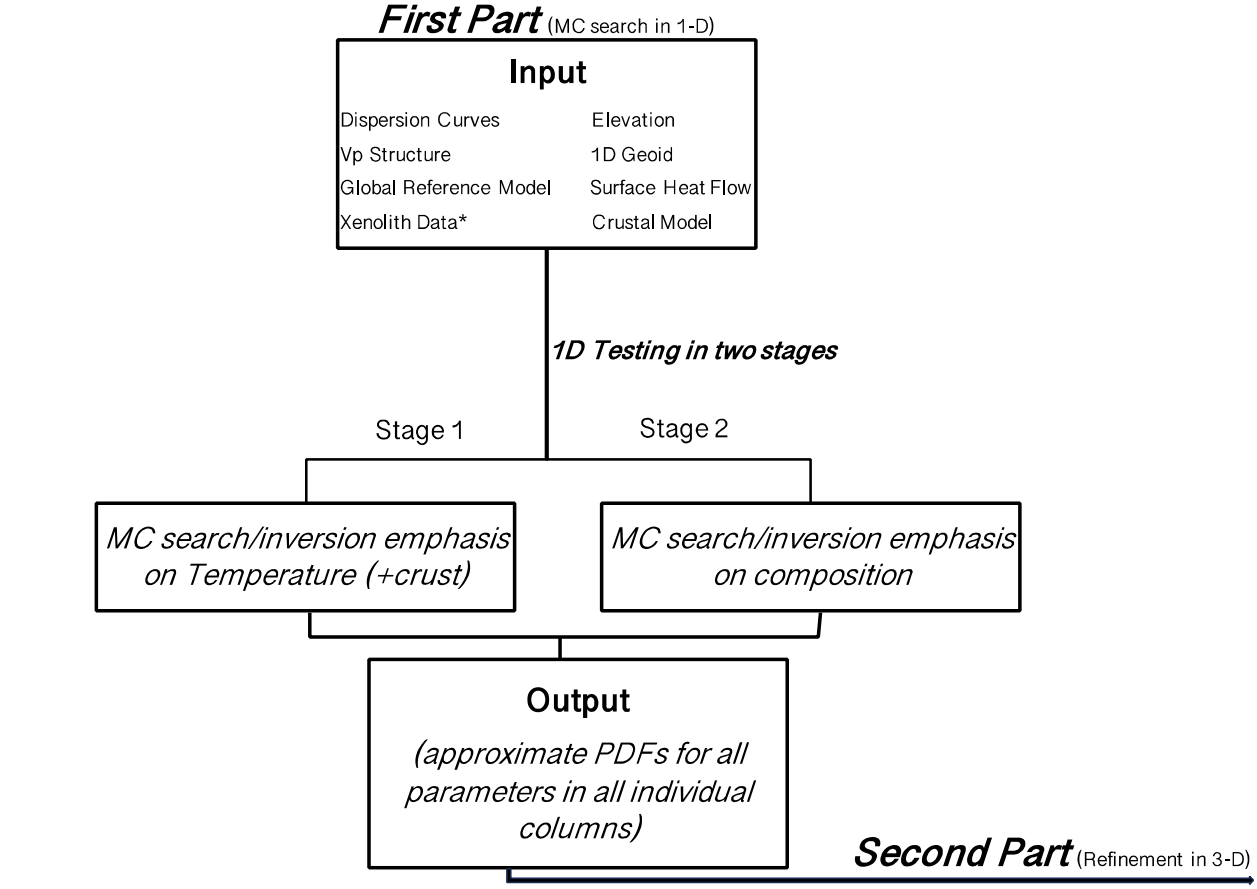

Figure 2. Flow chart illustrating the two-part inversion approach presented in this study.

3 Input

Seismic Datasets

- **Rayleigh wave dispersion data**

  The Rayleigh wave dispersion curves were extracted from phase velocity maps of a surface wave tomographic study conducted by Sharma et al., 2021. They obtained Rayleigh wave phase velocity maps at periods of 15-400 s, using a cross-correlation technique [23] to measure dispersion between pairs of stations across Canada. The study has local-scale resolution in many areas e.g., Hudson Bay and its surroundings, the eastern Canadian Shield, the central North American craton, and the western Canadian Cordilleran region and regional-scale resolution in the rest of the region.

  The data from regions with lower resolution ($> 3^{o}$) will be combined with data from an isotropic global upper mantle and transition zone velocity model SL2013sv [24]. This model is constrained by 521,705 vertical component broad-band seismograms and is based on a linearized (perturbation) inversion scheme. We subsequently subdivided the study region into 1027 nodes, each representing a surface area of 100 km $\times$ 100 km and extracted 1-D Rayleigh wave dispersion curves from the phase velocity maps at each node in the period range of 20 - 220 s which is linearly interpolated

from the data and is kept the same for the entire region. Since, the techniques employed to calculate the dispersion curves are least-squares inversions, the approximate though realistic uncertainties are scaled to period and kept the same for every grid node. We also visually inspected all dispersion curves in various geological provinces to identify any issues arising from the merging of the datasets. Figure 3 illustrates examples of input dispersion curves in each of the 5 geological provinces.

- **Body wave data**

  Our body wave data is extracted from CAP22 which is an absolute P-wave speed tomographic model with a focus on North America, specifically Canadian and Alaskan mantle structure [25]. It is an adaptively parameterized, global absolute P-wave tomographic model following the methodology of [26]. This data comprises 202,719 total absolute arrival-time data picks from temporary seismograph stations across Canada and Alaska where the phases include P, Pn, Pg, pP, PKP, and PKIKP. Since the technique employed is a least-squares inversion method, we employ approximate but realistic uncertainties which are scaled depth-wise and tested for various geological provinces and latitudes. Further discussion of these uncertainties is addressed in Section 4. Figure 3 illustrates P-wave input data for representative grid nodes in the 5 geological provinces.

- **Global reference model**

  We utilize a 3-D model of mantle shear-wave speeds, compressional-wave speeds and density called GyPSuM as our global reference model at deeper mantle depths [27]. This helps account for velocity and density anomalies in the deeper mantle and restricts their effects on the shallower structures constrained by our model. The GyPSuM P-wave and S-wave input data for the 5 geological provinces are shown in Figure 3.

Non-Seismic Datasets

- **Elevation**

  We took the elevation data from the ETOPO1 model (`https://www.ngdc.noaa.gov/mgg/global/global.html`, Figure 4a), filtered with a low-pass filter to remove the high-frequency content (wavelengths $<$ 50 km). The means and their variances for elevation are then computed for each 100 km $\times$ 100 km cell from their original data sets. The means become the input values used in the inversion, while the variances provide an estimation of the natural variability of the field within each cell. In most cases, the variances so obtained are 150 m.

- **Geoid**

  Geoid has long been recognized as having a better sensitivity to deep density anomalies and variations of the lithosphere-asthenosphere boundary (LAB) than gravity anomalies [17; 28]. The geoid height data for the Superior province project were extracted from the global Earth Geopotential Model EGM2008 [29], which includes spherical harmonic coefficients up to degree and order 2190. However, it contains dominant effects of deep ($>$ 400 km) mantle anomalies that we do not consider in the inversion and that, therefore, need to be removed. We applied a high-pass filter to the full geoid data to remove degrees and orders 2 – 9 [19; 30; 31; 32; 33]. However, for our current project, we need to consider that these are the same wavelengths which are also sensitive to the difference between continents and oceans. While the EGM2008 works for continental-lithosphere-only regions, we need to be cautious since we will be mapping continental shelf as well as transitional zones between continental lithosphere and oceanic lithosphere in Northern Canada (Innuitian Orogen).

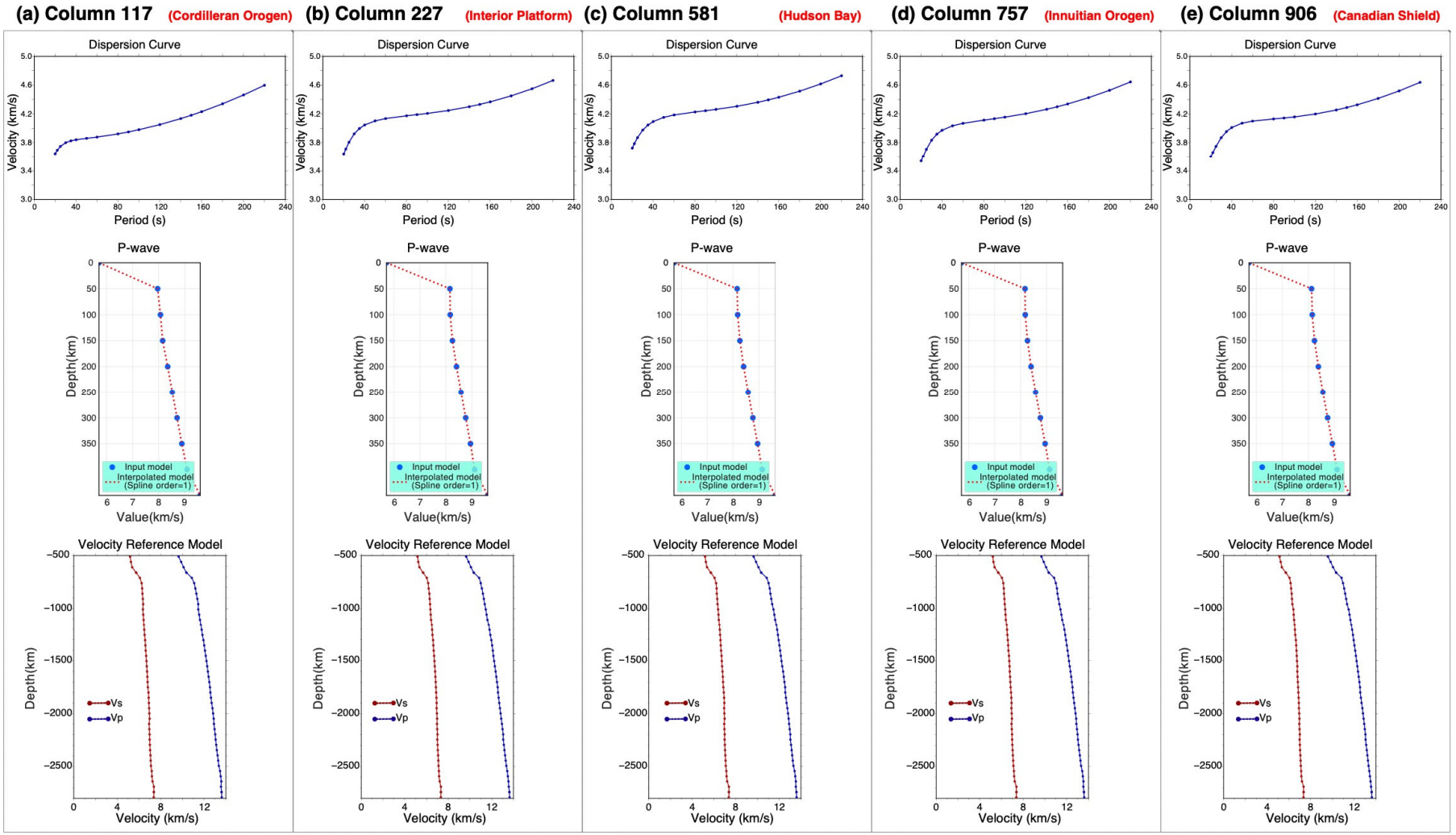

Figure 3. (a), (b), (c), (d), and (e) Input models of dispersion curve data, P-wave data, and the global reference model for five representative grid nodes in various geological provinces. The locations of these grid nodes are shown in Fig. 1(b).

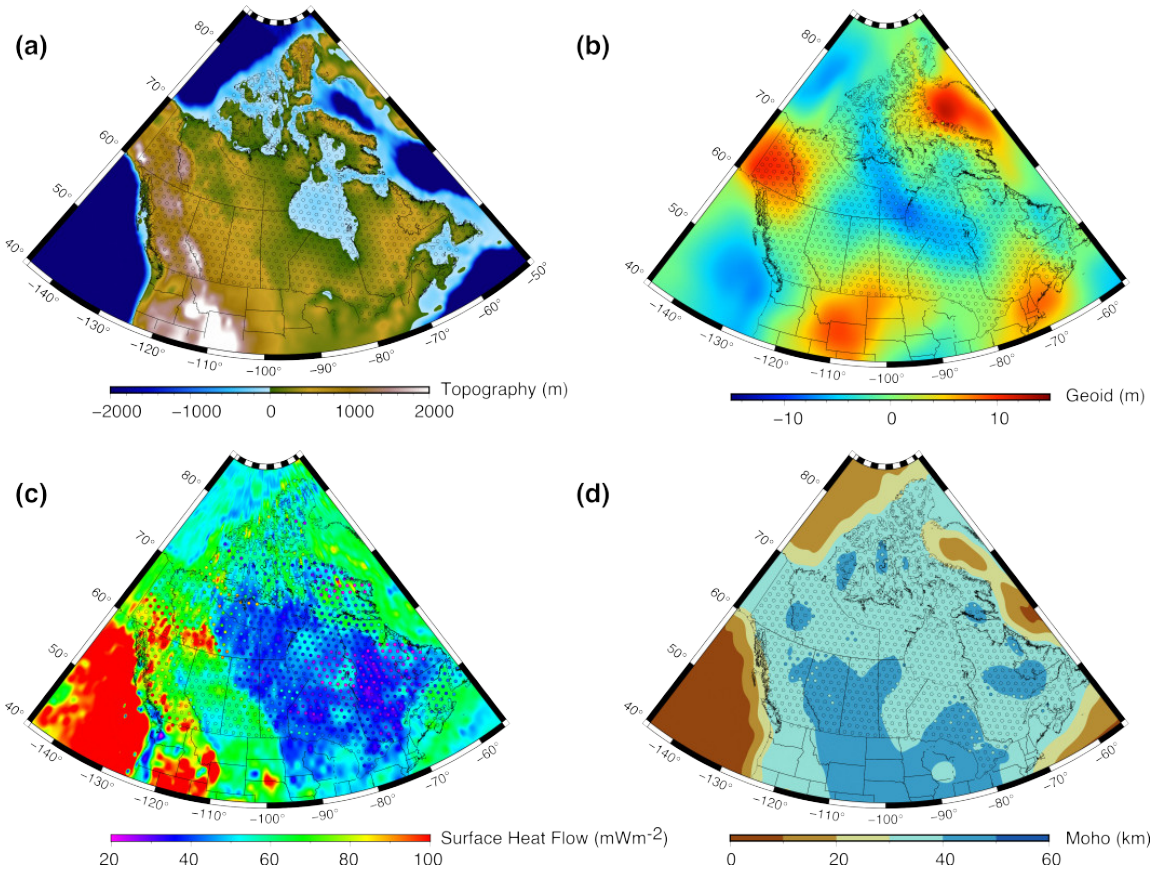

Figure 4. Input models for (a) Elevation, (b) Geoid, (c) Surface heat flow, and (d) Moho depth. The circles denote the 1027 grid nodes and the colour of the circle denotes the value at that node. The colour scale for the grid node data and the background input model are the same to show consistency in extraction and interpolation.

Hence, we utilized the latest Upper Mantle Geoid model UMG3 [34] which uses spherical harmonic analysis and recent tomography and density models from joint seismic-geodynamic inversions to derive a representative upper mantle geoid, including the contributions from low harmonic degrees Figure 4b. To account for both measurement variability and theoretical modelling errors (especially those associated with the solution of the forward problems), we assign minimum uncertainty to a geoid height of 1.5 m [17; 30; 32; 33; 35].

- **Surface Heat Flow**

Surface heat flow (SHF) measurements suffer from a scarcity and uneven distribution of data due to their high cost, especially in continental regions [36]. These measurements primarily reflect crustal heat production and are significantly influenced by shallow advection processes, while their sensitivity to deep mantle thermal anomalies diminishes beyond depths of 180 km [37]. Consequently,

relying solely on SHF data to construct lithospheric/sub-lithospheric models is considered unreliable. Nevertheless, SHF measurements provide valuable but limited insights and can be considered as a supplementary observation for understanding the mantle's thermal structure. In this regard, the weight assigned to SHF data in the inversion process is relatively low compared to other observables like seismic waves. However, any plausible model of the upper mantle and lithosphere must still be consistent with the available SHF data [36].

The SHF dataset for the region has been compiled from the Global Heat Flow Database which is the global compilation of the world heat flow data. It is a collaborative project between academia and industry to provide authenticated and exhaustive heat flow data for the understanding of Earth's thermal field. We interpolated the dataset onto the study grid and following the arguments in [30; 32], we removed some outliers with values < 20 mWm^{-2} or > 150 mWm^{-2}, as they are likely affected by local underground water circulation and thus cannot be representative of the deeper geotherm Figure 4c.

We will be using geological information to constrain areas with poor data coverage and the associated uncertainties in the 1-D testing part of this project. Typical uncertainties associated with SHF measurements in continents amount to 5 – 15 mWm^{-2} [38], which is equivalent to a depth change in the LAB of 50 km (if the LAB is defined as an isotherm, e.g., 1300 ºC). However, this equivalency is strictly valid only if the LAB change is confined to a depth range between 60 - 180 km. At 250 km depth, an identical change in depth translates into a SHF change of only 5 – 8 mW m^{-2}.

Our ability to reproduce real data is greatly limited by measurement errors and uncertainties in the structure of the mathematical models (e.g., 1-D approximation). Assuming Gaussian statistics for observational and theoretical/modeling errors, a single minimum uncertainty value (strictly, a covariance matrix) that accounts for both sources of error can be obtained [18; 39]. The minimum uncertainties (standard deviation) assigned to topography, geoid height, and heat flow are based on the detailed uncertainty analysis presented and discussed in [18].

- **Crustal model**

Our study domain is made up of a collection of adjacent and non-overlapping 1-D columns forming a 100 km × 100 km grid. Each of these columns making up our model has either two or three crustal layers based on sediments being absent or present (sediments, crystalline layer 1, and crystalline layer 2) and three mantle layers (lithospheric layers 1 and 2 and sub-lithospheric mantle). The initial thicknesses of the crustal layers and Moho depth are taken from the latest Earth crustal model ECM1 [40] Figure 4d. These thicknesses are subsequently modified, within their respective priors, during the Markov Chain Monte Carlo (MCMC) inversion and their values are ultimately given by the posterior PDF.

Each crustal layer is characterized by six layer-specific parameters: thickness, bulk density at surface Pressure-Temperature conditions, V_p / V_s ratio, coefficient of thermal expansion (α), thermal conductivity (κ) and compressibility (β) along with the radiogenic heat production (RHP) (see Tables 1 and 2). Of these parameters, only the first three along with RHP are regarded as unknowns in the inversion, whereas the others (α, κ, and β) are assumed to be known and constant. This choice is based on previous studies [19] which conclusively showed that the inversion results are highly sensitive to the 'unknown' four parameters and are only mildly sensitive to realistic variations on the other 'known' three.

To keep the parameter space as restricted as possible, we only consider the average RHP of the entire crust in the inversion. The initial velocities and densities of the crustal layers are taken from [40].

Table 1. The depth to the LAB (lithospheric thickness) and the bulk composition of the mantle layers within the CFMAS system (CaO, FeO, MgO, Al_2O_3 and SiO_2) complete the vector of model parameters to invert for.

Table 1	
Model Parameters	Range
Crust	
STP density (first crustal layer (sediments), kg/m^3)	1,700 – 2,800
STP density (second crustal layer, kg/m^3)	2,500 – 2,950
STP density (third crustal layer, kg/m^3)	2,600 – 3,150
V_p/V_s (first crustal layer (sediments))	1.60 – 4.10
V_p/V_s (second crustal layer)	1.60 – 1.95
V_p/V_s (third crustal layer)	1.60 – 1.95
Thickness perturbation (first crustal layer (sediments), km)	- 0.05 – 0.05
Thickness perturbation (second crustal layer, km)	- 5.0 – 5.0
Thickness perturbation (third crustal layer, km)	- 5.0 – 5.0
RHP ($\mu W/m^3$)	- 0.1 – 2.0
Mantle	
LAB depth (km)	170 – 330
Al_2O_3 in the lithosphere (wt. %)	0.2 – 4.0
FeO in the lithosphere (wt. %)	6.0 – 9.2
MgO in the lithosphere (wt. %)	34.0 – 55.0
CaO in the lithosphere (wt. %)	0.15 – 4.0
Al_2O_3 in the sub lithosphere (wt. %)	2.5 – 4.5
FeO in the sub lithosphere (wt. %)	6.0 – 9.2
MgO in the sub lithosphere (wt. %)	34.0 – 55.0
CaO in the sub lithosphere (wt. %)	0.5 – 4.5
T_{buffer} (°C)	1,240 - 1,600
T_{inter} (°C)	1,300 – 1,700
T_{bottom} (°C)	1,350 – 1,750

Table 2	
Constant Crustal Parameters	
Parameters	Values
α (first crustal layer (sediments), 1/°C)	2.3×10^{-5}
α (second crustal layer, 1/°C)	2.3×10^{-5}
α (third crustal layer, 1/°C)	2.3×10^{-5}
κ (first crustal layer (sediments), W $m^{-1}.°C^{-1}$)	1.5
κ (second crustal layer, W $m^{-1}.°C^{-1}$)	2.4
κ (third crustal layer, W $m^{-1}.°C^{-1}$)	2.4
β (first crustal layer (sediments), 1/Pa)	4.0×10^{-11}
β (second crustal layer, 1/Pa)	2.0×10^{-11}
β (third crustal layer, 1/Pa)	1.2×10^{-11}

Table 2. α = coefficient of thermal expansion, κ = thermal conductivity, and β = compressibility.

4 1-D Testing

As explained in the previous section, the entire inversion is based on an MCMC approach and in the first exploratory stage, we subdivide the 3-D volume into individual 1-D rectangular columns and invert a subset of the entire data vector in each column using observables that are most sensitive to the 1-D subsurface structure (i.e., dispersion curves, surface heat flow, geoid height under a 1-D approximation, and absolute elevation assuming lithospheric isostasy). In this 1-D grid-wise testing phase, we focus purely on constraining reliable and robust bounds and uncertainties for our 1-D inversion input parameters. This phase will have no structural or compositional interpretation of the lithospheric mantle.

Figure 5 shows the full set of outputs generated from the inversion at a representative grid node. The search in the first stage involves testing by trial the theoretical uncertainties assigned to the forward solvers to ascertain the compensation for the 1-D approximation and to avoid over-restricting the parameter space with a special focus on the temperature. During this stage, the LAB depth bounds are kept within a wide range of $50 < \text{LAB} < 380$ km which is large enough to include most of the variability commonly thought to exist in continental lithosphere [41; 42]. We will be testing the following individually and sequentially: (1) V_p uncertainties, (2) SHF data uncertainties, (3) Moho, (4) Lithospheric discontinuities i.e., Mid-Lithospheric Discontinuity (MLD), and (5) Thermal Parameters.

As an example of this process, Figure 6 illustrates the testing scenario associated with V_p uncertainties. The red dashed line in the figure shows the extent of the Superior Province area covered previously. Since the uncertainties have already been tested for the latitudinal extent of this region, bearing in mind the type of geological area covered (i.e., majorly cratonic) we are testing for the range of theoretical uncertainties which can be assigned to the V_p data based on depth as well as latitude.

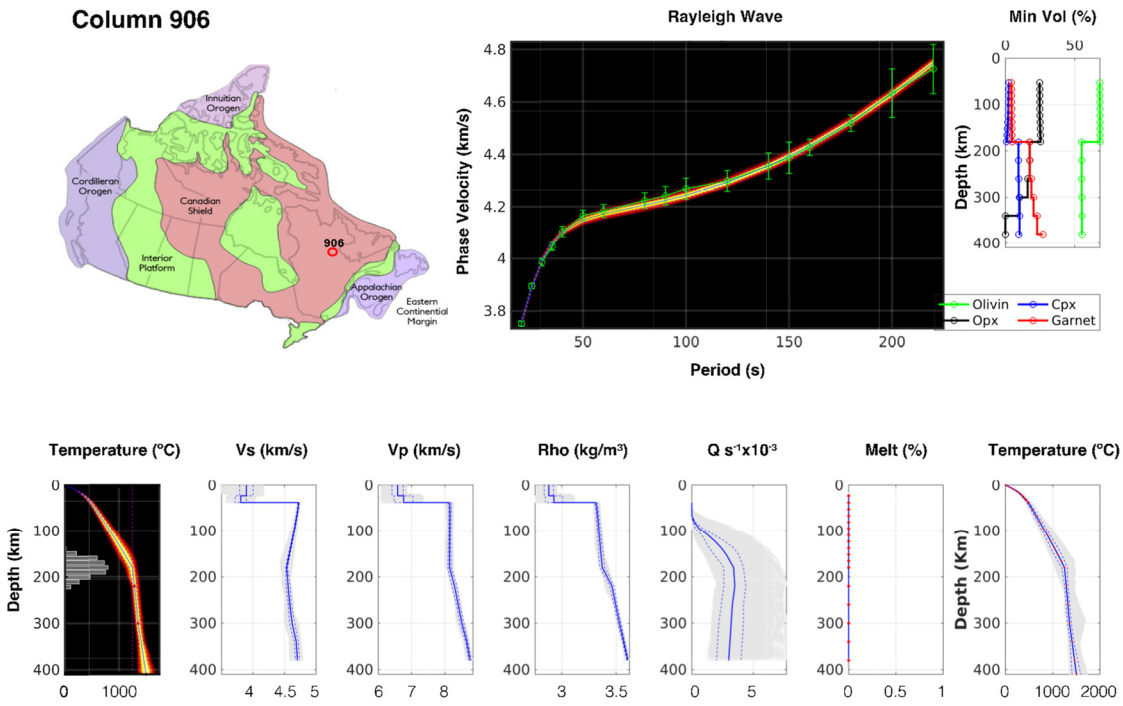

Figure 5. Example of a full set of 1-D output from inversion at grid node 906. The location is shown in the upper left-hand image.

The body wave data (CAP22) can be divided into two lateral areas with the model resolving fine-scale structures in the south (< 60 °N) and course-scale structures in the north (> 60 °N). Due to the inherent nature of the ray path of P-waves, the resolution can again vary as a function of depth based on ray coverage, less-well-resolved topmost depths < 100 km and well-resolved lower depths > 100 km. The test value of uncertainties ranges from smaller values assigned to well-resolved regions and depths to higher values assigned to less-well-resolved regions and depths.

In Figure 6, the four black solid circles denote the test grid nodes located in the Cordilleran region with a latitudinal spacing of ~0.5°. The three nodes located at and below 60 °N show a good fit-to-data and a good percentage of acceptable models with an uncertainty value of 0.14 km/s. The fourth node located at 65 °N yielded a very poor percentage of acceptance and fit to data for uncertainty values 0.14 km/s and 0.16 km/s but showed significant improvement for 0.18 km/s.

On further testing the uncertainty values by depth, it doesn't show any change in the percentage of acceptable models or fit-to-data. This allows us to affix a value of 0.18 km/s for V_p data at all grid nodes above 60 °N in the Cordilleran region and at all depths as a starting input model.

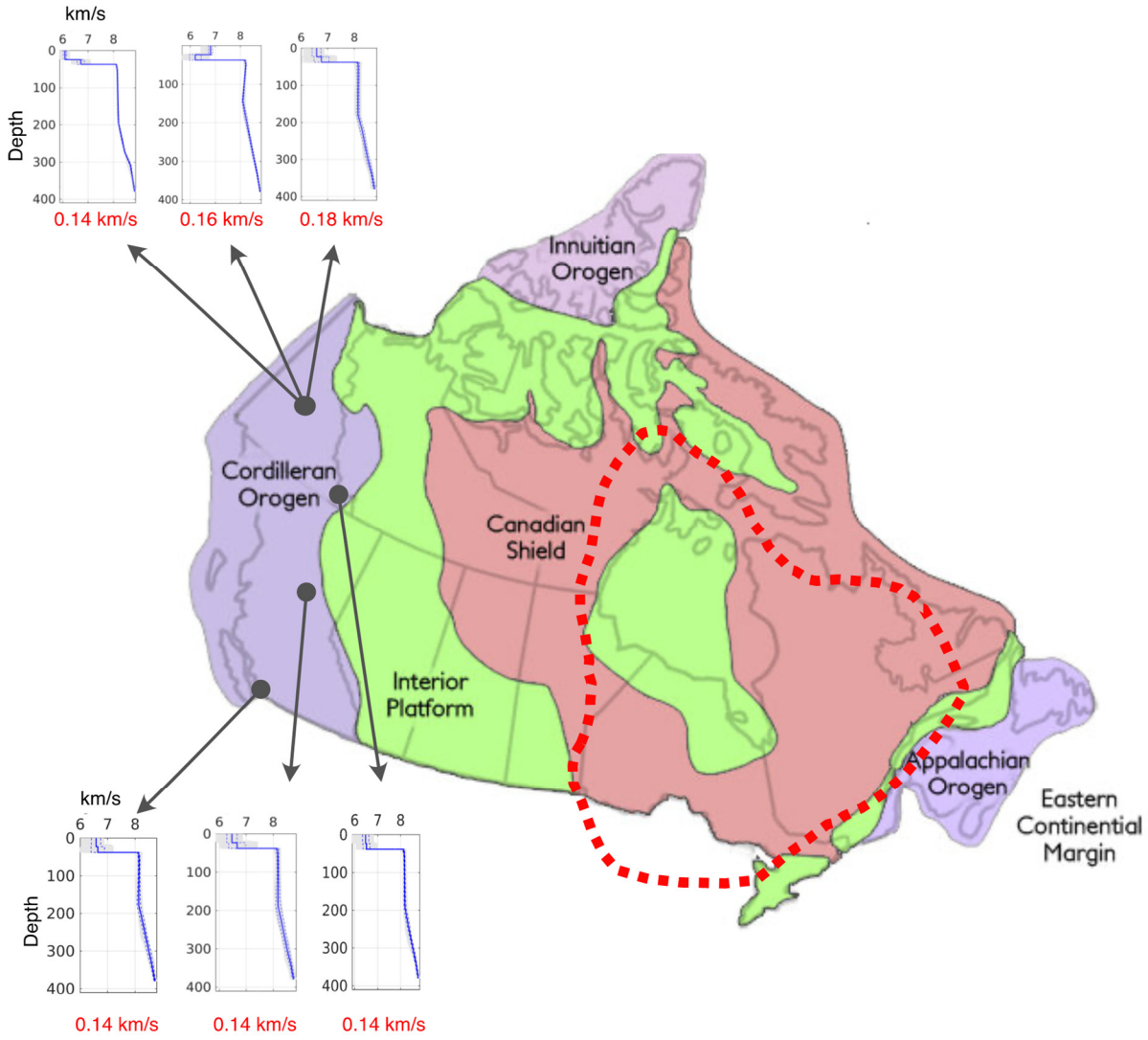

Figure 6. The black solid circles denote the four grid nodes for testing the V_p misfit to ascertain the appropriate value of uncertainties in the input model. The black arrows point to the predicted V_p plots recovered at these grid nodes with the red text denoting the assigned uncertainty values.

5 Future Work

(i) Once we have refined the 1-D testing with a focus on thermal structure, we will generate the samples of the average composition of the lithosphere by restricting the bounds of lithospheric discontinuities. This is necessary to avoid the potential, though unlikely, problem which can arise if the actual average lithospheric composition is significantly different from the assumed one. In this case, the inversion can compensate for the large compositional contrast with relatively large and unrealistic variations in the LAB or in the internal thermal structure of the lithosphere.
(ii) At the end of testing, we will be constructing a pseudo-3D model of the region from the refined 1-D outputs at every grid node which will bring us to the end of the first stage of this project.
(iii) The second stage will comprise joint inversion to constrain the 3D thermal and compositional structure independently.

References

1. Whitmeyer, S. J. & Karlstrom, K. E. Tectonic model for the Proterozoic growth of North America. *Geosphere* **3**, 220–259, DOI: 10.1130/GES00055.1 (2007).

2. Fulton, R. J. *Quaternary geology of Canada and Greenland* (Geological Society of America, 1989).

3. Vincent, J. S. Quaternary geology of the southeastern canadian shield. (1989).

4. Wheeler, J. & GSC. *Geological map of Canada: Map 1860A* (1996).

5. Hoffman, P. United plates of America, the birth of a craton: Early Proterozoic assembly and growth of Laurentia. *Annual Review of Earth and Planetary Sciences* **16**, 543–603, DOI: 10.1146/annurev.ea.16.050188.002551 (1988).

6. St-Onge, M., Searle, M. & Wodicka, N. Trans-Hudson Orogen of North America and Himalaya-Karakoram-Tibetan Orogen of Asia: Structural and thermal characteristics of the lower and upper plates. *Tectonics* **25**, TC4006, DOI: 10.1029/2005TC001907 (2006).

7. Hynes, A. & Rivers, T. Protracted continental collision—Evidence from the Grenville orogen. *Canadian Journal of Earth Sciences* **47**, 591–620, DOI: 10.1139/E10-003 (2010).

8. Doin, M.-P., Fleitout, L. & McKenzie, D. Geoid anomalies and the structure of continental and oceanic lithospheres. *Journal of Geophysical Research: Solid Earth* **101**, 16119–16135, DOI: 10.1029/96JB00640 (1996).

9. Griffin, W., O'Reilly, S. Y., Afonso, J. C. & Begg, G. The composition and evolution of lithospheric mantle: a re-evaluation and its tectonic implications. *Journal of Petrology* **50**, 1185–1204, DOI: 10.1093/petrology/egn033 (2009).

10. Begg, G. *et al.* The lithospheric architecture of africa: Seismic tomography, mantle petrology, and tectonic evolution. *Geosphere* **5**, 23–50 (2009).

11. Crow, R. *et al.* Shrinking of the colorado plateau via lithospheric mantle erosion: Evidence from nd and sr isotopes and geochronology of neogene basalts. *Geology* **39**, 27–30 (2011).

12. Hasterok, D. & Chapman, D. S. Continental thermal isostasy: 2. application to north america. *Journal of Geophysical Research: Solid Earth* **112** (2007).

13. Levandowski, W., Jones, C. H., Shen, W., Ritzwoller, M. H. & Schulte-Pelkum, V. Origins of topography in the western us: Mapping crustal and upper mantle density variations using a uniform seismic velocity model. *Journal of Geophysical Research: Solid Earth* **119**, 2375–2396 (2014).

14. Jones, C. H., Mahan, K. H., Butcher, L. A., Levandowski, W. B. & Farmer, G. L. Continental uplift through crustal hydration. *Geology* **43**, 355–358 (2015).

15. Molnar, P., England, P. C. & Jones, C. H. Mantle dynamics, isostasy, and the support of high terrain. *Journal of Geophysical Research: Solid Earth* **120**, 1932–1957 (2015).

16. Haxby, W. & Turcotte, D. On isostatic geoid anomalies. *Journal of Geophysical Research: Solid Earth* **83**, 5473–5478 (1978).

17. Afonso, J. *et al.* 3-D multiobservable probabilistic inversion for the compositional and thermal structure of the lithosphere and upper mantle. I: A priori petrological information and geophysical observables. *Journal of Geophysical Research: Solid Earth* **118**, 2586–2617, DOI: 10.1002/jgrb.50124 (2013).

18. Afonso, J. C., Fullea, J., Yang, Y., Connolly, J. & Jones, A. 3-D multi-observable probabilistic inversion for the compositional and thermal structure of the lithosphere and upper mantle. II: General methodology and resolution analysis. *Journal of Geophysical Research* **118**, 1650–1676, DOI: 10.1002/jgrb.50123 (2013b).

19. Afonso, J. C. *et al.* 3-D multiobservable probabilistic inversion for the compositional and thermal structure of the lithosphere and upper mantle: III. Thermochemical tomography in the Western-Central US. *Journal of Geophysical Research: Solid Earth* **121**, 7337–7370, DOI: 10.1002/2016JB013049 (2016).

20. Dave, R., Darbyshire, F., Afonso, J. C. & Fomin, I. Thermochemical structure of the superior craton and environs: Implications for the evolution and preservation of cratonic lithosphere. *Geochemistry, Geophysics, Geosystems* **25**, e2024GC011454 (2024).

21. Riddhi, D. & Schaeffer, A. Developing thermochemical models of canada's lithosphere. In *International Kimberlite Conference: Extended Abstracts*, vol. 12 (2024).

22. Fomin, I., Afonso, J. C., Gorbatov, A., Salajegheh, F. & Dave, R. Multi-observable thermochemical tomography: new advances and applications to the superior and north australian cratons., DOI: 10.22541/essoar.172070620.01240765/v1 (2024).

23. Meier, T., Dietrich, K., Stockhert, B. & Harjes, H.-P. One-dimensional models of shear wave velocity for the eastern Mediterranean obtained from the inversion of Rayleigh wave phase velocities and tectonic implications. *Geophysical Journal International* **156**, 45–58, DOI: 10.1111/j.1365-246X.2004.02121.x (2004).

24. Schaeffer, A. & Lebedev, S. Global shear speed structure of the upper mantle and transition zone. *Geophysical Journal International* **194**, 417–449, DOI: 10.1093/gji/ggt095 (2013).

25. Boyce, A. *et al.* A New P-Wave Tomographic Model (CAP22) for North America: Implications for the Subduction and Cratonic Metasomatic Modification History of Western Canada and Alaska. *Journal of Geophysical Research: Solid Earth* **128**, e2022JB025745 (2023).

26. Li, C., van der Hilst, R., Engdahl, E. & Burdick, S. A new global model for P wave speed variations in Earth's mantle. *Geochemistry, Geophysics, Geosystems* **9**, DOI: 10.1029/2007GC001806 (2008).

27. Simmons, N. A., Forte, A. M., Boschi, L. & Grand, S. P. GyPSuM: A joint tomographic model of mantle density and seismic wave speeds. *Journal of Geophysical Research* **115**, DOI: 10.1029/2010JB007631 (2010).

28. Afonso, J., Fernandez, M., Ranalli, G., Griffin, W. & Connolly, J. Integrated geophysical-petrological modelling of the lithospheric-sublithospheric upper mantle: methodology and applications. *Geochemistry, Geophysics, Geosystems* **9**, DOI: 10.1029/2007GC001834 (2008).

29. Pavlis, N. K., Holmes, S. A., Kenyon, S. C. & Factor, J. K. The development and evaluation of the Earth Gravitational Model 2008 (EGM2008). *Journal of Geophysical Research* **117**, DOI: 10.1029/2011JB008916 (2012).

30. Guo, Z. *et al.* Seismic evidence of on-going sublithosphere upper mantle convection for intra-plate volcanism in Northeast China. *Earth and Planetary Science Letters* **433**, 31–43, DOI: 10.1016/j.epsl.2015.09.035 (2016).

31. Qashqai, M. T., Afonso, J. C. & Yang, Y. Physical state and structure of the crust beneath the Western-Central United States from multiobservable probabilistic inversion. *Tectonics* **37**, 3117–3147, DOI: 10.1029/2017TC004914 (2018).

32. Shan, B. *et al.* The thermochemical structure of the lithosphere and upper mantle beneath south China: Results from multiobservable probabilistic inversion. *Journal of Geophysical Research: Solid Earth* **119**, 8417–8441, DOI: 10.1002/2014JB011412 (2014).

33. Zhang, A. *et al.* The deep lithospheric structure of the Junggar terrane, NW China: Implications for its origin and tectonic evolution. *Journal of Geophysical Research: Solid Earth* **124**, 11615–11638, DOI: 10.1029/2019JB018302 (2019).

34. Salajegheh, F. & Afonso, J. The upper mantle geoid for lithospheric structure and dynamics. *Journal of Geophysical Research: Solid Earth* **128**, e2023JB026397 (2023).

35. Yang, Y. Application of teleseismic long-period surface waves from ambient noise in regional surface wave tomography: a case study in western usa. *Geophysical Journal International* **198**, 1644–1652 (2014).

36. Davies, J. H. & Davies, D. R. Earth's surface heat flux. *Solid earth* **1**, 5–24 (2010).

37. Jaupart, C. & Mareschal, J.-C. *Heat generation and transport in the Earth* (Cambridge university press, 2010).

38. Powell, W., Chapman, D., Balling, N. & Beck, A. Continental heat-flow density. *Handbook of Terrestrial Heat-Flow Density Determination: with Guidelines and Recommendations of the International Heat-Flow Commission* 167–222 (1988).

39. Tarantola, A. *Inverse problem theory and methods for model parameter estimation* (Society for Industrial and Applied Mathematics, Philadelphia, USA, 2005).

40. Mooney, W. D., Barrera-Lopez, C., Suárez, M. G. & Castelblanco, M. A. Earth crustal model 1 (ecm1): A 1 x 1 global seismic and density model. *Earth-Science Reviews* 104493 (2023).

41. Pasyanos, M. E. Lithospheric thickness modeled from long-period surface wave dispersion. *Tectonophysics* **481**, 38–50 (2010).

42. Fishwick, S. Surface wave tomography: imaging of the lithosphere–asthenosphere boundary beneath central and southern africa? *Lithos* **120**, 63–73 (2010).